ACS NANO

www.acsnano.org

ARTICLE

Direct View of Gate-Tunable Miniband Dispersion in Graphene Superlattices Near the Magic Twist Angle

Zhihao Jiang, Dongkyu Lee, Alfred J. H. Jones, Youngju Park, Kimberly Hsieh, Paulina Majchrzak, Chakradhar Sahoo, Thomas S. Nielsen, Kenji Watanabe, Takashi Taniguchi, Philip Hofmann, Jill A. Miwa, Yong P. Chen, Jeil Jung, and Søren Ulstrup*

Cite This: *ACS Nano* 2025, 19, 2379–2387

Read Online

ACCESS | Metrics & More | Article Recommendations | Supporting Information

ABSTRACT: **Superlattices from twisted graphene mono- and bilayer systems give rise to on-demand many-body states such as Mott insulators and unconventional superconductors. These phenomena are ascribed to a combination of flat bands and strong Coulomb interactions. However, a comprehensive understanding is lacking because the low-energy band structure strongly changes when an electric field is applied to vary the electron filling. Here, we gain direct access to the filling-dependent low-energy bands of twisted bilayer graphene (TBG) and twisted double bilayer graphene (TDBG) by applying microfocused angle-resolved photoemission spectroscopy to in situ gated devices. Our findings for the two systems are in stark contrast: the doping-dependent dispersion for TBG can be described in a simple model, combining a filling-dependent rigid band shift with a many-body-related bandwidth change. In TDBG, on the other hand, we find a complex behavior of the low-energy bands, combining nonmonotonous bandwidth changes and tunable gap openings, which depend on the gate-induced displacement field. Our work establishes the extent of electric field tunability of the low-energy electronic states in twisted graphene superlattices and can serve to underpin the theoretical understanding of the resulting phenomena.**

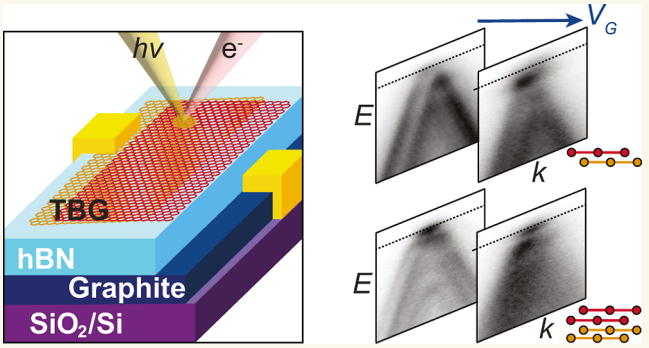

KEYWORDS: *twisted bilayer graphene, moiré superlattice, flat bands, microARPES, in situ gating, bandwidth renormalization*

INTRODUCTION

Stacking two graphene layers with a small interlayer twist angle θ gives rise to a long-range moiré structure and brings the linearly dispersing Dirac states at the Brillouin zone (BZ) corners within close vicinity of each other. In twisted bilayer graphene (TBG), hybridization between the Dirac states leads to the formation of low-energy bands in the resulting moiré mini-Brillouin zone (mBZ). In contrast to the high-velocity Dirac states, these low-energy "minibands" consist of hole-like lower branches (LB) and electron-like upper branches (UB) that are essentially flat. Additionally, the opening of hybridization gaps separates the LB and UB from the continua of bands below the valence band maximum (VBM) and above the conduction band minimum (CBM),[1−3] as sketched in Figure 1a. The electron filling in the flat minibands can be widely tuned by applying a vertical electric field. The resulting changes in the carrier density, n, can shift the Fermi level in a hybridization band gap and induce an insulating state.[3,4] As an alternative to graphene layers, a twisted heterostructure can also be formed by two Bernal-stacked bilayers of graphene. In this material, twisted double bilayer graphene (TDBG), the minibands arise from two hyperbolic bands with electric field-tunable band gaps (see Figure 1b),[5−9] leveraging a wider field-tunability of the minibands.[10−13] Near the "magic" twist angle, $\theta \approx 1.1°$, the minibands become extremely flat such that the Coulomb interaction U dominates over the kinetic energy, as measured by the bandwidth W. In this condition, half-integer filling levels of the minibands trigger correlated insulator states in both TBG and TDBG.[10,14]

Received: September 13, 2024
Revised: December 16, 2024
Accepted: December 23, 2024
Published: January 9, 2025

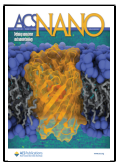

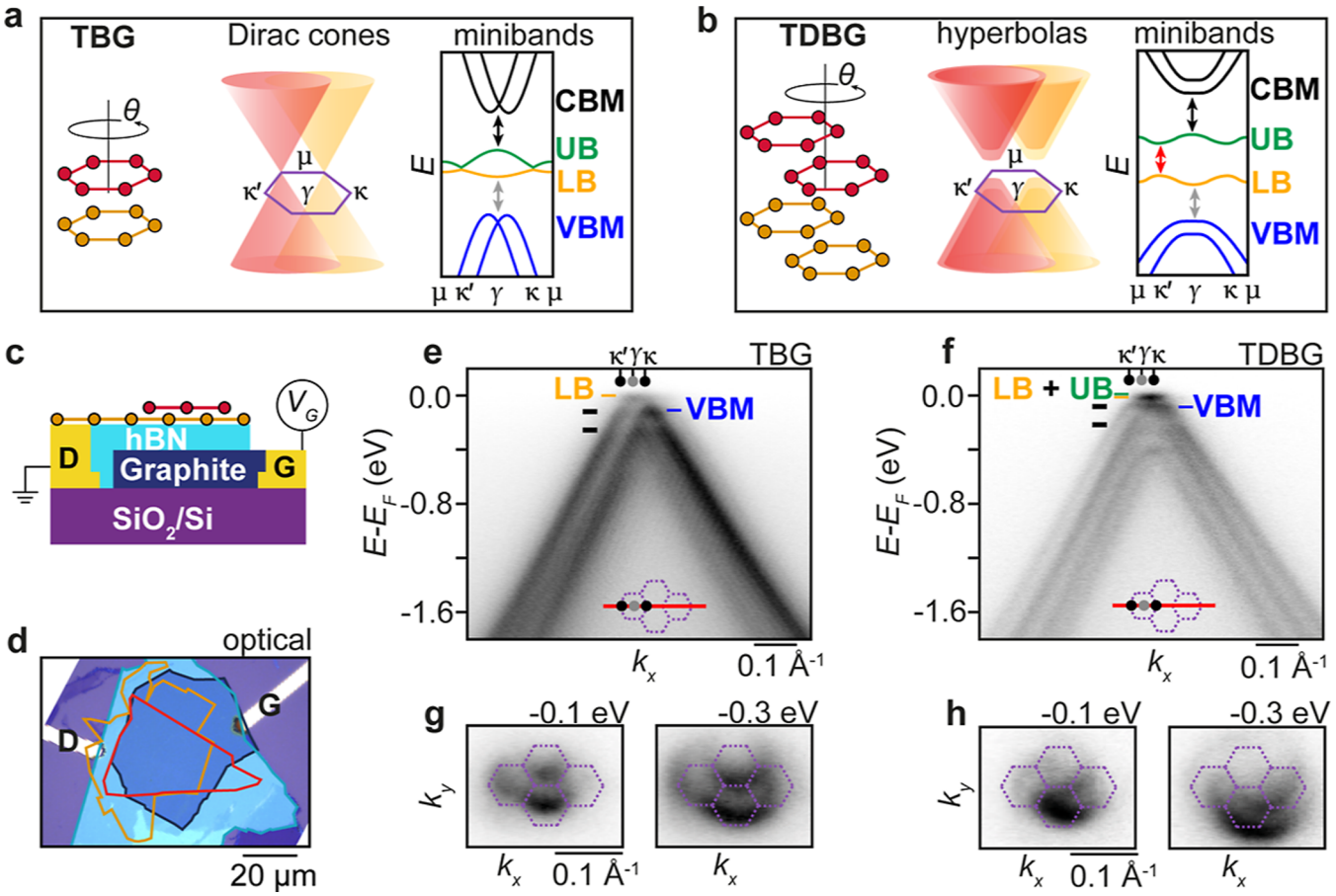

Figure 1. Electronic structure of devices composed of twisted bilayer (TBG) and double bilayer graphene (TDBG) near the magic twist angle. (a,b) Outline of mBZs around overlapping (a) Dirac cones originating from top (red) and bottom (orange) graphene layers of TBG and (b) hyperbolic bands centered on top (red) and bottom (orange) Bernal-stacked graphene bilayers of TDBG. The miniband dispersion is sketched in each case, providing an overview of our definitions of CBM, UB, LB, and VBM. Band gaps are demarcated by double-headed arrows. (c) Schematic illustration of device architecture. (d) Optical micrograph of TBG device. Top graphene, bottom graphene, hBN, and graphite gate are demarcated by red, orange, light blue, and dark blue outlines, respectively. Drain and gate electrodes are labeled (D,G), respectively. (e,f) ARPES spectra of (e) TBG and (f) TDBG along the $\kappa'-\gamma-\kappa-\mu-\kappa'$ direction indicated by a red line in the mBZ diagrams. The high symmetry points κ and κ' are demarcated by black circles, while γ is indicated by a gray circle. (g,h) Constant energy surfaces of (g) TBG and (h) TDBG at −0.1 eV and −0.3 eV. The extracted energies are marked by black ticks in (e,f). The LB, UB, and VBM are marked by orange, green, and blue ticks, respectively.

Due to the prominent role of many-body effects, changing the carrier density does not simply lead to a rigid shift of the minibands but rather to a complex change of the band dispersion. This is to be expected because the presence of van Hove singularities in the miniband dispersion can drastically affect the many-body effects when the dispersion is tuned to the Fermi level. The resulting spectral functions are extremely challenging to address theoretically.[15−18] Experimentally, direct access to the doping-dependent miniband dispersion around the magic angle has not been achieved but signatures of miniband pinning due to van Hove singularities and symmetry-breaking cascade transitions have been observed in scanning tunneling spectroscopy experiments.[19−23] We gain direct access to the miniband $E(k)$-dispersion by applying angle-resolved photoemission spectroscopy with micrometer spatial resolution (microARPES) to TBG and TDBG near the magic twist angle.[24−28] Crucially, the experiments of the present study are carried out in an optimum device geometry for photoemission spectroscopy, such that we can resolve the detailed energy- and momentum-dependent spectral function at variable displacement field and electron doping, and thereby directly access the many-body-induced band deformations that result from long-range Coulomb interactions as the filling of minibands is tuned by a gate voltage.[29]

RESULTS AND DISCUSSION

Electronic Structure of TBG and TDBG Devices. A sketch and an optical micrograph of our TBG sample are presented in Figure 1c,d. A graphite back gate, demarcated by a dark blue outline, is placed on SiO_2/Si and encompasses the majority of the area with twisted graphene layers, with each graphene monolayer indicated by orange and red outlines. A hexagonal boron nitride (hBN) layer with a thickness around 30 nm, demarcated by a light blue outline, is sandwiched between graphite and graphene flakes. The top layers are grounded via a drain (D) electrode, while a voltage is applied via the gate (G) electrode to the graphite. Our TDBG device was constructed following the same architecture. Simplified diagrams of our device design are presented together with detailed microARPES intensity maps and corresponding optical images for the TBG and TDBG samples in Figure S1. Both devices contain regions of bare monolayer and

https://doi.org/10.1021/acsnano.4c12905
ACS Nano 2025, 19, 2379−2387

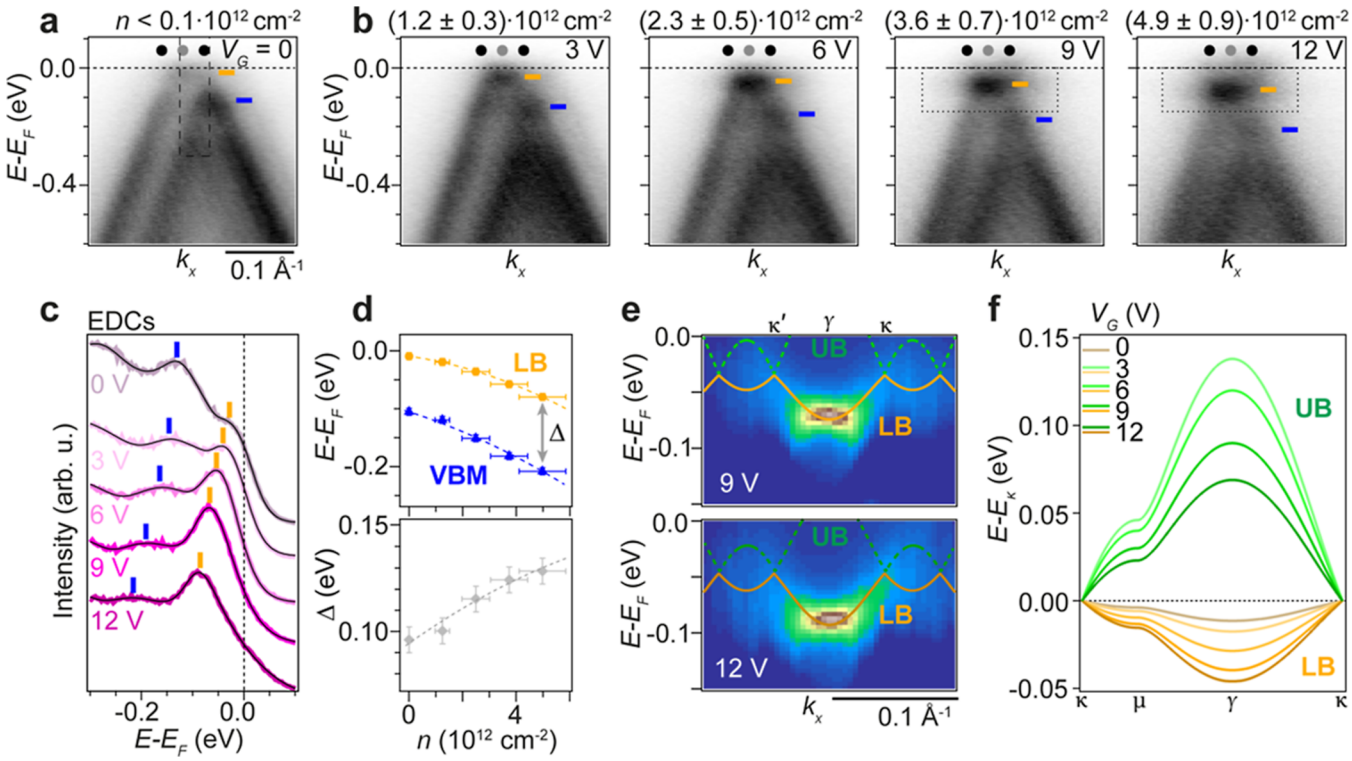

Figure 2. Gate-tunable electronic structure of TBG. (a,b) ARPES spectra along $\kappa'-\gamma-\kappa-\mu-\kappa'$ of TBG obtained at the stated values of gate voltage and carrier density. Black and gray circles indicate κ, κ', and γ points as defined in Figure 1e. (c) EDCs integrated over a k-range of 0.04 Å^{-1}, as indicated by a dashed box in (a), and fits (smooth thin curves) to Lorentzian peaks multiplied by the Fermi−Dirac function at the stated gate voltages below the curves. Fitted peak positions corresponding to LB and VBM are demarcated by orange and blue ticks, respectively. (d) Top panel: fitted peak positions from the EDC analysis in (c). Bottom panel: extracted values of the LB-VBM peak-to-peak energy difference Δ. The dashed lines represent polynomial fits that have been added as a guide to the eye. (e) Curvature plots of the ARPES intensity within the rectangular (E, k)-window outlined at 9 V and 12 V in (b). The overlaid LB and UB dispersion are results of a fit to the curvature intensity, as described in Figure S5 and Methods. (f) Fitted LB and UB dispersion relative to the κ-point energy at the measured gate voltages.

Bernal-stacked bilayer graphene directly above the graphite back-gate electrode. ARPES spectra from these regions are used to calibrate the carrier concentration, n, induced by the gate voltage V_G (see Figures S2 and S3). The twist angle in the devices is $\theta = (1.2 \pm 0.2)°$, as verified by conductive tip atomic force microscopy (C-AFM) measurements (see Figure S4).[30]

Figure 1e−h presents $E(k)$-dispersion cuts and constant energy surfaces for (e,g) TBG and (f,h) TDBG at zero gate voltage. The dispersion cuts in panels (e,f) have been extracted along the high symmetry $\kappa'-\gamma-\kappa-\mu-\kappa'$ direction, which is indicated by a red line in the mBZ sketches. The κ', κ, and γ points are demarcated by black and gray circles, respectively. In the case of TBG in panel (e), we observe a faint flat band at the Fermi energy, which we identify as the LB (see orange tick). We can resolve the LB state straddling the Fermi energy despite the low initial carrier concentration in our TBG device, which is below our accuracy level of 1×10^{-11} cm^{-2}, because our measurement is performed at room temperature, leading to sufficient thermal excitation of the band. The VBM is identified below the LB at an energy of −0.1 eV (see blue tick). The $E(k)$-dispersion of TDBG in panel (f) displays an intense flat state at the Fermi level, which we interpret as being composed of the adjacent LB and UB states (see orange and green ticks), which initially appear gapless due to our resolution limitations, as described in the Methods section. These bands are separated from segments of interacting hyperbolic bands that define the flat VBM (see blue tick). The carrier density at zero gate voltage for our TDBG device is determined to be $(1.4 \pm 0.3) \times 10^{12}$ cm^{-2}, such that there is substantial occupation and thus photoemission intensity from both LB and UB straddling the Fermi energy. The constant energy surfaces in panels (g,h) are extracted at −0.1 eV and −0.3 eV, respectively, cutting through segments of the VB states that are separated by a hybridization gap in both materials. This leads to intensity being concentrated in the center of mBZs at −0.1 eV and spiraling outward toward the mBZ edges at −0.3 eV, providing a guide to construct the mBZs (see dotted hexagons) from the ARPES intensity. In both cases, we estimate a reciprocal moiré lattice vector length of 0.06 Å^{-1}, which is consistent with the twist angle obtained from C-AFM.

Gate Tuning of Bandwidth in TBG. The gate-dependent dispersion along $\kappa'-\gamma-\kappa-\mu-\kappa'$ of our TBG device is presented in Figure 2a,b. The positions of LB and the VBM are tracked in Figure 2c by fitting energy distribution curves (EDCs) integrated over a k-range of 0.04 Å^{-1} corresponding to the $\gamma - \kappa$ region encompassing LB and VB states, as indicated by a dashed box in Figure 2a. Note that this analysis gives the energy of highest photoemission intensity, which coincides with the band position only for a truly flat band, inducing some uncertainty in the case of dispersive states. As the gate voltage and carrier density are increased, LB shifts to lower energy and becomes more intense (see orange tick mark that tracks the LB based on the EDC fits). The VBM also shifts to lower energy and diminishes in intensity (see blue tick mark that tracks the

https://doi.org/10.1021/acsnano.4c12905
ACS Nano 2025, 19, 2379−2387

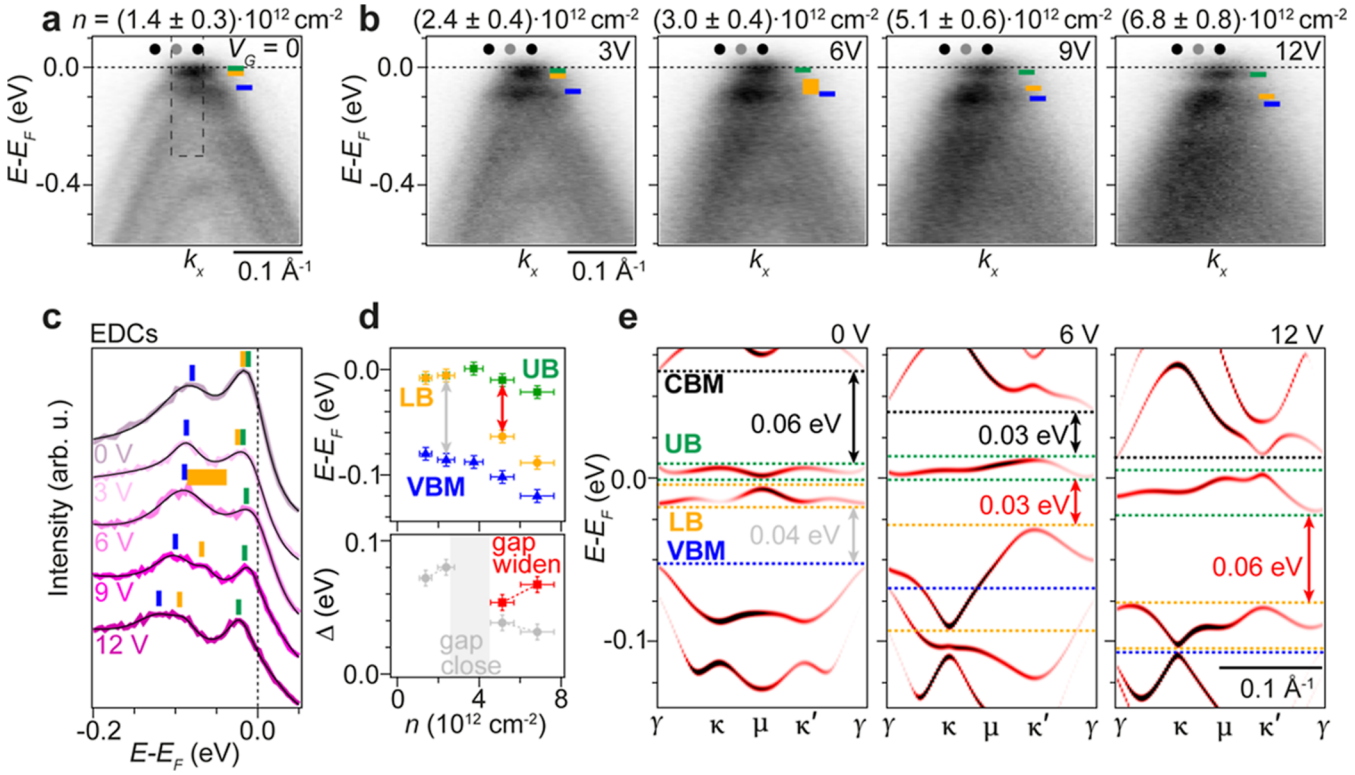

Figure 3. Gate-tunable electronic structure of TDBG. (a,b), ARPES spectra along $\kappa'-\gamma-\kappa-\mu-\kappa'$ of TDBG at the stated values of gate voltage and carrier density. Black and gray circles indicate κ, κ', and γ points as defined in Figure 1f. (c) EDCs (colored curves) extracted over a k-range of 0.04 Å^{-1} as indicated by the dashed box in (a) and fits (smooth curves) to Lorentzian peaks multiplied by the Fermi−Dirac function at the stated gate voltages. Orange, green, and blue ticks demarcate peak positions corresponding to LB, UB, and VBM, respectively. The peak positions are also indicated in (a,b). Note that the LB and UB are indistinguishable at 0 and 3 V. (d) Top panel: fitted peak positions of UB, LB, and VBM from the EDC analysis. Bottom panel: peak-to-peak energy separations between LB and VBM (gray markers), as well as LB and UB (red markers). (e) Calculated spectral functions at the given V_G. CBM and VBM offsets are marked by horizontal black and blue dashed lines, respectively. UB and LB are encompassed by horizontal green and orange dashed lines, respectively. Double-headed black, gray, and red arrows demarcate CBM-UB, LB-VBM, and UB-LB band gaps, respectively.

VBM based on EDC fits). These shifts are summarized in the top panel of Figure 2d. The LB-VBM peak-to-peak energy difference Δ, which characterizes the hybridization gap, is calculated as a function of n from the fits and presented in the bottom panel of Figure 2d, revealing an increase on the order of 30 meV from depleted to occupied flat bands. This increasing hybridization gap is an important observation for the potential many-body effects in this material because the enhanced energy separation reduces interband interactions.

A detailed analysis of the miniband dispersion within a narrow (E, k)-window, demarcated by dotted rectangles at 9 V and 12 V in Figure 2b, is presented in Figure 2e and Figure S5. The spectra have been determined by applying the curvature method to the raw ARPES intensity, which enhances the faint miniband dispersion.[31] We identify the intense flat band segment as the minimum of the LB at γ and the upward dispersing segments as the dispersion toward the κ- and κ'-points. We find that the UB cannot be fully occupied before reaching the saturation point for doping in our device. We thus merely observe the intensity from the UB spilling below the Fermi energy, touching the LB at κ- and κ'. The complete LB dispersion is captured by fitting the hopping parameter t_{LB} and band offset E_0 in a two-band tight binding model for a honeycomb lattice to the peak curvature intensity (see Figure S5 and Methods). It has been overlaid as an orange curve in Figure 2e. The curvature intensity continues uninterrupted into the UB states and we find no indication of a gap formation in the observed filling range with our experimental resolution (see Methods).

We estimate the bandwidth of the UB dispersion by requiring the carrier density that can be calculated from the tight binding model to be identical to the experimentally determined values at a given gate voltage (see Methods for further details). The resulting gate-dependent miniband dispersion is plotted relative to the κ-point energy in Figure 2f. The UB bandwidth is generally larger than that for the LB. Furthermore, we observe that the LB widens, while the UB flattens as the doping increases. Both observations are consistent with many-body calculations and experiments.[15−18,23] Indeed, similar many-body effects have been shown via ARPES to drive band flattening of the π-band in single-layer graphene.[29]

Doping- and Field-Dependent Dispersion of TDBG. Figure 3a,b presents the gate-tunable ARPES dispersion along $\kappa'-\gamma-\kappa-\mu-\kappa'$ of TDBG. Similarly as for TBG, we extract VBM, LB, and UB band positions from EDC analysis in Figure 3c and track the fitted positions via blue, orange, and green tick marks, respectively. The n-dependence of peak energies is presented in the top panel of Figure 3d. Peak-to-peak energy separations, shown via gray and red double-headed arrows, represent LB-VBM and UB-LB hybridization gaps, respectively. Their values have been plotted in the bottom panel of Figure 3d. Initially, the LB and UB states are not possible to disentangle within the main flat band intensity at the Fermi

https://doi.org/10.1021/acsnano.4c12905
ACS Nano 2025, 19, 2379−2387

level due to the resolution limitations of our experiment (see Methods). The fitted EDC peak is therefore composed of both nondegenerate but closely spaced bands when the gate voltage is set between 0 V and 3 V. A hybridization gap on the order of 75 meV is observed toward the VBM in this low-voltage regime. At 6 V, we measure intensity that is continuously filling the gapped region toward the VBM. Upon further doping, intensity is again depleted from the gapped region, and two closely spaced peaks are observable around −0.1 eV. These are interpreted as the LB and VBM with a strongly suppressed hybridization gap, compared to the initial situation. A UB-LB hybridization gap on the order of 50 meV is observable at 9 V and increases to 70 meV upon further increasing the doping and displacement field at 12 V. The general trend of an increasing displacement field between graphene layers driving an increasing gap between flat bands is in line with observations from transport experiments.[10]

These observations and, in particular, the difficulty of observing the LB at a gating voltage of 6 V can be understood by comparison to spectral function calculations within a Coulomb interaction-corrected tight-binding model (see Methods for more details), as shown in Figure 3e and Figure S6. The (E, k)-dependence of the calculated spectral weight originates from the sublattice weights in the band unfolding procedure, as described in Methods. The calculations were carried out using the experimental value of hBN thickness of 30 nm and applied a saw-like external potential corresponding to the experimental gate voltages. The calculations thereby take into account the effect of the displacement field in the gated device structure, simulating the effect of the on-site interaction energies being varied. The significant asymmetry and shifting of the bands observed in Figure 3e and Figure S6 therefore stem from a varying displacement field, as the doping is tuned. The resulting spectral function at 0 V reveals two closely spaced LB and UB minibands, consistent with the ARPES data. Gaps of 60 meV and 40 meV separate the UB and LB from the CBM and VBM, respectively. As the gate voltage is tuned, the flat bands separate by up to 60 meV at 12 V, and the remaining gaps decrease or vanish entirely. The LB and UB initially display similar narrow bandwidths. As the displacement field is varied by increasing the voltage to 6 V, the LB acquires substantial dispersion and shifts to lower energy while the UB remains pinned around the Fermi energy. The LB then flattens again as it shifts further down upon further increasing the gate voltage. This behavior matches our experimental observation of intensity filling the gapped region at 6 V, precluding a clear observation of the LB. We have therefore marked the LB via a widened tick mark at 6 V in Figure 3b,c. The theory also explains the re-emergence of the narrow LB peak at 9 V and 12 V in the ARPES data by the reflattening of the LB state seen in the calculations. The substantial band broadening of the LB leads to the LB-VBM gap closing in the intermediate doping range, as illustrated in the bottom panel of Figure 3d. By contrast, the UB-LB gap at high doping agrees well with the calculated value because both bands are narrow, and the determined peak position thus corresponds well to the band center.

CONCLUSIONS

Our findings underline the vast design freedom in moiré systems by revealing a striking difference in the doping- and displacement field-dependent band dispersion of TBG and TDBG. The behavior of TBG is nontrivial in the sense that the minibands experience a nonrigid shift upon increased electron doping, corresponding to a monotonous bandwidth change of the LB and UB in opposite directions (see Figure 4a).

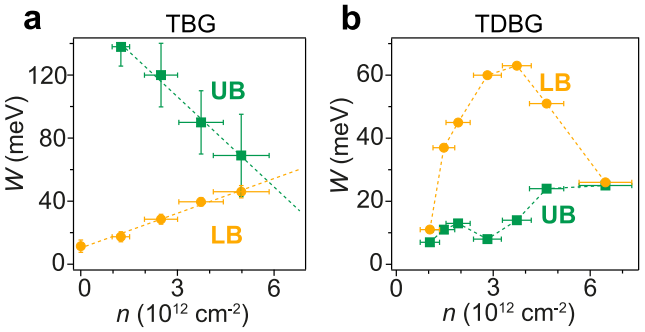

Figure 4. Bandwidth renormalization with doping in TBG and TDBG. (a) LB and UB bandwidths obtained from the fitted TBG dispersions in Figure 2f. Dashed lines are linear fits that have been added as a guide to the eye. (b) LB and UB bandwidths of TDBG extracted from the calculated spectral functions in Figure 3e and Figure S6.

However, this is easily captured by a simple tight-binding model with a variable hopping parameter t. Moreover, the results are consistent with the theoretically expected behavior[15,16,18] and previous experiments on single-layer graphene.[29] By contrast, the doping and field-dependent band dispersion observed in TDBG are highly complex. The LB and UB bandwidth changes determined from the calculated spectral function are summarized in Figure 4b. Upon increasing the doping and displacement field, all bands shift to lower energies, but they also drastically change their dispersion with a nonmonotonous bandwidth change. This tunable bandwidth ultimately influences the U/W ratio in the LB and UB that leads to Mott insulating and superconducting phases at low temperatures. At doping levels where the correlated insulator phase emerges in the LB, we find bandwidths in the range of 10−20 meV for both TBG and TDBG. In the doping regime where correlation effects emerge in the UB, we estimate somewhat larger bandwidths, on the order of 60 meV and 20 meV for TBG and TDBG, respectively. These values reflect the complex doping- and field-dependent asymmetries between the flat band dispersions that underpin the electronic phase diagrams of moiré superlattice systems composed from twisted graphene layers.[32]

METHODS

Fabrication of Devices. Stacking of 2D flakes was accomplished using the dry-transfer technique applying polymers.[33,34] Graphene and hBN layers were exfoliated onto the SiO_2/Si substrates. Their size and thickness were identified by optical microscopy and AFM. Bilayer and monolayer graphene flakes were cut in two pieces by using a sharp tip with a 2 μm diameter. One of the pieces was picked up using a polycarbonate (PC)/polydimethylsiloxane (PDMS) stamp mounted on a glass slide at 130 °C. The remaining piece was rotated by an angle θ,[4] which was set 0.1° higher than the target angle and stacked with the mono- or bilayer graphene flake on the stamp in order to form TBG or TDBG. Then, an hBN flake with a thickness around 30 nm was picked up at 120 °C, which was followed by picking up a graphite flake at 130 °C to be used as a back gate. Finally, the stack was released onto SiO_2/Si with Au/Cr-patterned electrodes based on 50 nm gold and 5 nm chromium films at 180 °C. Twisted graphene layers and back gates were contacted by different electrodes.

https://doi.org/10.1021/acsnano.4c12905
ACS Nano 2025, 19, 2379−2387

Heterostructures were then annealed in a H_2/Ar environment at 250 °C for several hours prior to measurement.

C-AFM Measurements. Conductive tip (C-AFM) measurements were performed in an inert N_2 atmosphere (<1 ppm of H_2O and O_2) using a commercial Asylum Research Cypher S AFM integrated into a Jacomex GP(Concept) glovebox. To preserve the twist angles, samples were measured immediately after performing microARPES measurements, without any further annealing or cleaning treatments. C-AFM scans were performed using doped-diamond-coated conductive tips (NanoSensors CDT-CONTR). A bias voltage was applied to the sample via a series resistance of 1 GΩ to limit the current through the sample. The average periodicity of the moiré patterns was extracted using Gwyddion software and determined to be $\theta = (1.2 \pm 0.2)°$.

microARPES Measurements. The microARPES measurements were performed at the SGM4 beamline of the ASTRID2 light source at Aarhus University, Denmark.[35] The devices were wire bonded to CSB00815 chip carriers and annealed in the microARPES end-station at a temperature of 180 °C for 1 h before exposure to the beam. Throughout the data collection, the samples were kept at room temperature in a base pressure better than 2×10^{-10} mbar.

The synchrotron beam with a photon energy of 47 eV was focused to a spot size of 4 μm using an elliptical capillary mirror [Sigray Inc.]. The ARPES spectra were obtained using a SPECS Phoibos 150 SAL analyzer. The total experimental energy-resolution stemming from the electron analyzer and beamline settings amounted to 35 meV, while the momentum resolution was 0.01 Å^{-1}. The scans of (E, k_x, k_y)-dependent photoemission intensity were acquired with the scanning angle lens mode of the analyzer while keeping the sample position fixed. The (E, k, x, y)-dependent data sets were obtained by rastering the sample position relative to the beam using a piezoelectric stage [SmarAct] and measuring an (E, k)-dependent snapshot at each point. The samples were aligned along the $\kappa'-\gamma-\kappa-\mu-\kappa'$ direction of the mBZ. Electrostatic doping of the devices in situ was achieved using Keithley 2450 source meters.

Spectral Function Calculations for TDBG. A fully relaxed crystal structure of TDBG was obtained in a molecular dynamics simulation using LAMMPS[36] software with REBO2[37] and exact exchange random phase approximation (EXX-RPA)-fitted DRIP potentials.[38] The relaxation was performed for a 1.35° twisted commensurate cell made with two AB-stacked bilayer graphenes with a lattice constant of a = 2.46 Å. We performed calculations for 14,408 carbon π-orbitals within the relaxed structure of moiré lattice length of 104.39 Å.

We employed the following self-consistent interaction-corrected tight-binding Hamiltonian to prevent double-counting of the Coulomb interactions.[39]

$$H = H^0 + \sum_{i\sigma} (U\Delta\rho_{ii\tilde{\sigma}} + \sum_j V_{ij}\Delta\rho_{jj})c^{\dagger}_{i\sigma}c_{i\sigma} \tag{1}$$

Here, $\Delta\rho$ denotes the disparity between the density matrices of H and the noncorrected Hamiltonian $H^0 = \sum_{ij\sigma} t_{ij} c^{\dagger}_{i\sigma} c_{j\sigma}$. The operator $c_{i\sigma}(c^{\dagger}_{i\sigma})$ is an electron annihilation(creation) operator, where σ denotes the spin index, and $\tilde{\sigma}$ signifies the spin in the opposite direction. The hopping parameters t_{ij} were determined using the scaled hybrid exponential model, which incorporates the effects of structure relaxation.[38] We assumed the onsite Hubbard parameter U = 5 eV. For intersite interactions V_{ij}, values of V_1 = 2 eV for first nearest neighbors and V_2 = 1 eV for second nearest neighbors were assumed in intralayer relations, while for interlayer relations, the Coulomb equation accounting for bonding length was employed, as $V_{ij} = 1/(\epsilon_r\sqrt{(a/2\sqrt{3})^2 + r_{ij}^2})$ with the relative permittivity $\epsilon_r = 6$.[40] The exchange interaction was disregarded to simplify the calculations; hence, the calculations were carried out at the self-consistent Hartree level. Each gate voltage was considered to be applied to tDBG on 30 nm hBN, with saw-like external potential and doping corresponding to the same dielectric constant. The Fermi level of the calculations has been matched to the experiment by comparing the integrated spectral weight with the Lorentzian peaks obtained from the EDC analysis in Figure 3c, as shown in Figure S7. The self-consistent calculations were performed with 5 × 5 grid k-points.

In this calculation, we used the band unfolding approach of ref 41 to calculate the spectral function of moiré supercell systems. The spectral function at a point k of graphene BZ unfolded from a K point of the moiré BZ can be represented through

$$A(k, E) = -\frac{1}{\pi}\frac{S_g}{S_m}\sum_{K,G,N}\delta_{k-G,K}\sum_s \omega^s_{KN}(k)\mathrm{Im}\left[\frac{1}{E - \epsilon_{KN} + i\eta}\right] \tag{2}$$

where G is the reciprocal lattice vector of the moiré structure, N is the band index of the moiré band, s denotes the sublattices, and the parameter η is a broadening term that accounts for energy uncertainty, which is set to 0.1 meV. S_g and S_m represent the area of graphene unit cell and the unit cell of the moiré pattern, respectively. The weight at each sublattice $\omega^s_{KN}(k,E)$ is

$$\omega^s_{KN}(k) = \sum_{I\in s, J\in s}\delta_{i(I),i'(J)}(C^{KN*}_I) \times C^{KN}_J e^{ik(T_s(I)-T_s(J))} \tag{3}$$

where I and J are the basis indices in the moiré structure, the $i(I)$ labels are the basis in the primitive cell of the sublattice redefined from I basis, and C^{KN}_I is the eigenvector component. The vector $T_s(I)$ is the displacement of the I-basis from the primitive cell by a certain number of lattice vectors.

Analysis of ARPES Data. EDC fits in Figures 2c and 3c were performed by using a function composed of multiple Lorentzian peaks on a constant background, which was multiplied by the Fermi–Dirac function. We have performed peak position fits using other models, such as Voigt and Gaussian profiles, as well as applying polynomial background functions with and without multiplication of the Fermi–Dirac function. The peak positions and peak-to-peak energy differences shown in Figures 2d and 3d represent the mean values resulting from these different peak fitting functions. The standard deviation resulting from the analysis is less than 1 meV in all cases, leading to error bars smaller than the marker sizes.

The contribution to the EDC peak error bars resulting from energy broadening is analyzed in Figure S8. We model the measured ARPES intensity of TDBG using the calculated spectral function, which is multiplied by the Fermi–Dirac function at room temperature and convoluted with Gaussian energy- and momentum-broadening functions. Since we are measuring at room temperature, the Fermi edge has a full-width half-maximum (fwhm) of approximately 100 meV, which causes the flat bands within this energy range around the Fermi energy to be partially populated and thereby measurable with ARPES. In addition to the known experimental energy broadening of ΔE = 35 meV, the application of electric fields can lead to additional energy and momentum broadening.[28] The spectral functions of the materials are also intrinsically broadened, primarily due to impurity scattering. The combination of these effects can lead to the effective energy broadening being more substantial than 35 meV. Our simulations in Figure S8 reveal the impact on the EDCs and the accuracy of the peak fitting in our experimental conditions. We find that this contributes a standard deviation uncertainty on all energy peak positions of 6 meV, leading to the shown error bars.

The ARPES spectra presented in the main paper show the gating-dependent dispersion changes along the $\kappa'-\gamma-\kappa-\mu-\kappa'$ direction of the mBZs, as described in Figure 1e,f. In Figure S9, we show additional cuts along $\mu-\gamma-\mu$, which reveal consistent energy shifts of the flat band segments in TBG and TDBG. Furthermore, in Figure S10, we examine the effect of applying negative gate voltages, which leads to the depopulation of the LB states and the VBM shifting toward the Fermi energy.

Error bars on carrier concentration n have been determined in connection with the doping calibrations, as described in the captions of Figures S2 and S3.

The miniband dispersion of TBG was obtained by fitting the curvature intensity in Figure S5 to a two-band tight binding model on a honeycomb lattice given by

https://doi.org/10.1021/acsnano.4c12905
ACS Nano 2025, 19, 2379–2387

$E_{LB(UB)}(k) = \alpha_{LB(UB)} t_{LB(UB)} \sqrt{3 + 2\cos(\lambda_s k) + 4\cos(\lambda_s k/2)} - E_0$ where $t_{LB(UB)}$ is the LB (UB) hopping parameter, $\alpha_{LB} = -1$, $\alpha_{UB} = 1$, E_0 is the band offset, and $\lambda_s = a/2 \sin(\theta/2)$. The value of λ_s was fixed according to the twist angle measured by C-AFM. The applied vertical electric field in the device modulates the on-site energies, leading to band shifts that are accounted for in the model via the offset E_0. The bandwidth of the upper flat band is constrained by the requirement that the integral $\int g(E, W) n_{FD}(E) dE$ should return the measured carrier density n. Here, $g(E, W)$ is the density of states of the fitted tight binding bands with bandwidth W, and n_{FD} is the Fermi–Dirac function at room temperature.

The error bars on the LB bandwidth in TBG are obtained from the goodness of the dispersion fits of the hopping parameter t_{LB} (see fits in Figure S5). Within our simple tight binding model, we can write $t_{UB} = W/3 - t_{LB}$ and thereby get the error bar on t_{UB} by propagating the error bars on W and t_{LB}. For TDBG, the error bars on W are associated with how accurately we can determine the band edges, which leads to error bars smaller than the data points.

ASSOCIATED CONTENT

Supporting Information

The Supporting Information is available free of charge at https://pubs.acs.org/doi/10.1021/acsnano.4c12905.

Device schematics, optical images, and corresponding photoemission intensity maps; calibration of carrier density in TBG device; calibration of carrier density in TDBG device; determination of moiré lattice parameter with AFM; extraction of gating-dependent miniband dispersion in TBG; calculated gating-dependent TDBG spectral functions; comparison of measured and calculated EDC peaks for gated TDBG; analysis of the influence of energy broadening and room temperature Fermi edge width on ARPES spectra of minibands; gating-dependent dispersion along the μ–γ–μ direction in the mBZ of TBG and TDBG; and ARPES spectra at negative gate voltages for TBG and TDBG (PDF)

AUTHOR INFORMATION

Corresponding Author

Søren Ulstrup − *Department of Physics and Astronomy, Interdisciplinary Nanoscience Center, Aarhus University, Aarhus C 8000, Denmark;* orcid.org/0000-0001-5922-4488; Email: ulstrup@phys.au.dk

Authors

Zhihao Jiang − *Department of Physics and Astronomy, Interdisciplinary Nanoscience Center, Aarhus University, Aarhus C 8000, Denmark;* orcid.org/0000-0002-4203-1062

Dongkyu Lee − *Department of Physics, University of Seoul, Seoul 02504, Korea; Department of Smart Cities, University of Seoul, Seoul 02504, Korea*

Alfred J. H. Jones − *Department of Physics and Astronomy, Interdisciplinary Nanoscience Center, Aarhus University, Aarhus C 8000, Denmark;* orcid.org/0000-0002-7930-0967

Youngju Park − *Department of Physics, University of Seoul, Seoul 02504, Korea*

Kimberly Hsieh − *Department of Physics and Astronomy, Interdisciplinary Nanoscience Center, Aarhus University, Aarhus C 8000, Denmark*

Paulina Majchrzak − *Department of Physics and Astronomy, Interdisciplinary Nanoscience Center, Aarhus University, Aarhus C 8000, Denmark*

Chakradhar Sahoo − *Department of Physics and Astronomy, Interdisciplinary Nanoscience Center, Aarhus University, Aarhus C 8000, Denmark*

Thomas S. Nielsen − *Department of Physics and Astronomy, Interdisciplinary Nanoscience Center, Aarhus University, Aarhus C 8000, Denmark*

Kenji Watanabe − *Research Center for Electronic and Optical Materials, National Institute for Materials Science, Tsukuba 305-0044, Japan;* orcid.org/0000-0003-3701-8119

Takashi Taniguchi − *Research Center for Materials Nanoarchitectonics, National Institute for Materials Science, Tsukuba 305-0044, Japan;* orcid.org/0000-0002-1467-3105

Philip Hofmann − *Department of Physics and Astronomy, Interdisciplinary Nanoscience Center, Aarhus University, Aarhus C 8000, Denmark*

Jill A. Miwa − *Department of Physics and Astronomy, Interdisciplinary Nanoscience Center, Aarhus University, Aarhus C 8000, Denmark*

Yong P. Chen − *Department of Physics and Astronomy, Interdisciplinary Nanoscience Center, Aarhus University, Aarhus C 8000, Denmark; Department of Physics and Astronomy and School of Electrical and Computer Engineering and Purdue Quantum Science and Engineering Institute, Purdue University, West Lafayette, Indiana 47907, United States*

Jeil Jung − *Department of Physics, University of Seoul, Seoul 02504, Korea; Department of Smart Cities, University of Seoul, Seoul 02504, Korea;* orcid.org/0000-0003-2523-0905

Complete contact information is available at: https://pubs.acs.org/10.1021/acsnano.4c12905

Notes

The authors declare no competing financial interest.

ACKNOWLEDGMENTS

The authors acknowledge funding from the Novo Nordisk Foundation (Project Grant NNF22OC0079960), the Danish Council for Independent Research, Natural Sciences under the Sapere Aude program (Grant Nos. DFF-9064-00057B and DFF-6108-00409) and under a Research Project grant (Grant No. 1026-00089B), the Aarhus University Research Foundation, and from VILLUM FONDEN under the Villum Investigator Program (Grant No. 25931). D.L. acknowledges support by the Korean Ministry of Land, Infrastructure and Transport (MOLIT) from the Innovative Talent Education Program for Smart Cities. J.J. acknowledges support from the Korean NRF grant no. NRF2020R1A5A1016518. C.S. acknowledges the Marie Sklodowska-Curie Postdoctoral Fellowship (proposal number 101059528). K.W. and T.T. acknowledge support from the JSPS KAKENHI (Grant Nos. 21H05233 and 23H02052) and World Premier International Research Center Initiative (WPI), MEXT, Japan. We acknowledge the Urban Big Data and AI Institute of the University of Seoul supercomputing resources (http://ubai.uos.ac.kr) and KISTI Grant No. KSC-2022-CRE-0514 made available for conducting the research reported in this paper.

REFERENCES

(1) Bistritzer, R.; MacDonald, A. H. Moiré bands in twisted double-layer graphene. *Proc. Natl. Acad. Sci. U.S.A.* **2011**, *108*, 12233–12237.

(2) Lopes dos Santos, J. M. B.; Peres, N. M. R.; Castro Neto, A. H. Continuum model of the twisted graphene bilayer. *Phys. Rev. B* **2012**, *86*, 155449.
(3) Cao, Y.; Luo, J. Y.; Fatemi, V.; Fang, S.; Sanchez-Yamagishi, J. D.; Watanabe, K.; Taniguchi, T.; Kaxiras, E.; Jarillo-Herrero, P. Superlattice-Induced Insulating States and Valley-Protected Orbits in Twisted Bilayer Graphene. *Phys. Rev. Lett.* **2016**, *117*, 116804.
(4) Kim, K.; DaSilva, A.; Huang, S.; Fallahazad, B.; Larentis, S.; Taniguchi, T.; Watanabe, K.; LeRoy, B. J.; MacDonald, A. H.; Tutuc, E. Tunable moiré bands and strong correlations in small-twist-angle bilayer graphene. *Proc. Natl. Acad. Sci. U.S.A.* **2017**, *114*, 3364−3369.
(5) Chebrolu, N. R.; Chittari, B. L.; Jung, J. Flat bands in twisted double bilayer graphene. *Phys. Rev. B* **2019**, *99*, 235417.
(6) Koshino, M. Band structure and topological properties of twisted double bilayer graphene. *Phys. Rev. B* **2019**, *99*, 235406.
(7) Choi, Y. W.; Choi, H. J. Intrinsic band gap and electrically tunable flat bands in twisted double bilayer graphene. *Phys. Rev. B* **2019**, *100*, 201402.
(8) Haddadi, F.; Wu, Q.; Kruchkov, A. J.; Yazyev, O. V. Moiré Flat Bands in Twisted Double Bilayer Graphene. *Nano Lett.* **2020**, *20*, 2410−2415.
(9) Burg, G. W.; Zhu, J.; Taniguchi, T.; Watanabe, K.; MacDonald, A. H.; Tutuc, E. Correlated Insulating States in Twisted Double Bilayer Graphene. *Phys. Rev. Lett.* **2019**, *123*, 197702.
(10) Cao, Y.; Rodan-Legrain, D.; Rubies-Bigorda, O.; Park, J. M.; Watanabe, K.; Taniguchi, T.; Jarillo-Herrero, P. Tunable correlated states and spin-polarized phases in twisted bilayer−bilayer graphene. *Nature* **2020**, *583*, 215−220.
(11) Liu, X.; Hao, Z.; Khalaf, E.; Lee, J. Y.; Ronen, Y.; Yoo, H.; Haei Najafabadi, D.; Watanabe, K.; Taniguchi, T.; Vishwanath, A.; Kim, P. Tunable spin-polarized correlated states in twisted double bilayer graphene. *Nature* **2020**, *583*, 221−225.
(12) Shen, C.; et al. Correlated states in twisted double bilayer graphene. *Nat. Phys.* **2020**, *16*, 520−525.
(13) He, M.; Li, Y.; Cai, J.; Liu, Y.; Watanabe, K.; Taniguchi, T.; Xu, X.; Yankowitz, M. Symmetry breaking in twisted double bilayer graphene. *Nat. Phys.* **2021**, *17*, 26−30.
(14) Cao, Y.; Fatemi, V.; Demir, A.; Fang, S.; Tomarken, S. L.; Luo, J. Y.; Sanchez-Yamagishi, J. D.; Watanabe, K.; Taniguchi, T.; Kaxiras, E.; Ashoori, R. C.; Jarillo-Herrero, P. Correlated insulator behaviour at half-filling in magic-angle graphene superlattices. *Nature* **2018**, *556*, 80−84.
(15) Guinea, F.; Walet, N. R. Electrostatic effects, band distortions, and superconductivity in twisted graphene bilayers. *Proc. Natl. Acad. Sci. U.S.A.* **2018**, *115*, 13174−13179.
(16) Rademaker, L.; Abanin, D. A.; Mellado, P. Charge smoothening and band flattening due to Hartree corrections in twisted bilayer graphene. *Phys. Rev. B* **2019**, *100*, 205114.
(17) Cea, T.; Walet, N. R.; Guinea, F. Electronic band structure and pinning of Fermi energy to Van Hove singularities in twisted bilayer graphene: A self-consistent approach. *Phys. Rev. B* **2019**, *100*, 205113.
(18) Goodwin, Z. A. H.; Vitale, V.; Liang, X.; Mostofi, A. A.; Lischner, J. Hartree theory calculations of quasiparticle properties in twisted bilayer graphene. *Electron. Struct.* **2020**, *2*, 034001.
(19) Choi, Y.; Kemmer, J.; Peng, Y.; Thomson, A.; Arora, H.; Polski, R.; Zhang, Y.; Ren, H.; Alicea, J.; Refael, G.; von Oppen, F.; Watanabe, K.; Taniguchi, T.; Nadj-Perge, S. Electronic correlations in twisted bilayer graphene near the magic angle. *Nat. Phys.* **2019**, *15*, 1174−1180.
(20) Jiang, Y.; Lai, X.; Watanabe, K.; Taniguchi, T.; Haule, K.; Mao, J.; Andrei, E. Y. Charge order and broken rotational symmetry in magic-angle twisted bilayer graphene. *Nature* **2019**, *573*, 91−95.
(21) Xie, Y.; Lian, B.; Jäck, B.; Liu, X.; Chiu, C.-L.; Watanabe, K.; Taniguchi, T.; Bernevig, B. A.; Yazdani, A. Spectroscopic signatures of many-body correlations in magic-angle twisted bilayer graphene. *Nature* **2019**, *572*, 101−105.
(22) Kerelsky, A.; McGilly, L. J.; Kennes, D. M.; Xian, L.; Yankowitz, M.; Chen, S.; Watanabe, K.; Taniguchi, T.; Hone, J.; Dean, C.; Rubio, A.; Pasupathy, A. N. Maximized electron interactions at the magic angle in twisted bilayer graphene. *Nature* **2019**, *572*, 95−100.
(23) Choi, Y.; Kim, H.; Lewandowski, C.; Peng, Y.; Thomson, A.; Polski, R.; Zhang, Y.; Watanabe, K.; Taniguchi, T.; Alicea, J.; Nadj-Perge, S. Interaction-driven band flattening and correlated phases in twisted bilayer graphene. *Nat. Phys.* **2021**, *17*, 1375−1381.
(24) Utama, M. I. B.; et al. Visualization of the flat electronic band in twisted bilayer graphene near the magic angle twist. *Nat. Phys.* **2021**, *17*, 184−188.
(25) Lisi, S.; et al. Observation of flat bands in twisted bilayer graphene. *Nat. Phys.* **2021**, *17*, 189−193.
(26) Li, Y.; Zhang, S.; Chen, F.; Wei, L.; Zhang, Z.; Xiao, H.; Gao, H.; Chen, M.; Liang, S.; Pei, D.; et al. Observation of Coexisting Dirac Bands and Moiré Flat Bands in Magic-Angle Twisted Trilayer Graphene. *Adv. Mater.* **2022**, *34*, 2205996.
(27) Nunn, J. E.; McEllistrim, A.; Weston, A.; Garcia-Ruiz, A.; Watson, M. D.; Mucha-Kruczynski, M.; Cacho, C.; Gorbachev, R. V.; Fal'ko, V. I.; Wilson, N. R. ARPES Signatures of Few-Layer Twistronic Graphenes. *Nano Lett.* **2023**, *23*, 5201−5208.
(28) Jiang, Z.; Hsieh, K.; Jones, A. J. H.; Majchrzak, P.; Sahoo, C.; Watanabe, K.; Taniguchi, T.; Miwa, J. A.; Chen, Y. P.; Ulstrup, S. Revealing flat bands and hybridization gaps in a twisted bilayer graphene device with microARPES. *2D Mater.* **2023**, *10*, 045027.
(29) Ulstrup, S.; Schüler, M.; Bianchi, M.; Fromm, F.; Raidel, C.; Seyller, T.; Wehling, T.; Hofmann, P. Manifestation of nonlocal electron-electron interaction in graphene. *Phys. Rev. B* **2016**, *94*, 081403.
(30) Zhang, L.; Wang, Y.; Hu, R.; Wan, P.; Zheliuk, O.; Liang, M.; Peng, X.; Zeng, Y.-J.; Ye, J. Correlated States in Strained Twisted Bilayer Graphenes Away from the Magic Angle. *Nano Lett.* **2022**, *22*, 3204−3211.
(31) Zhang, P.; Richard, P.; Qian, T.; Xu, Y.-M.; Dai, X.; Ding, H. A precise method for visualizing dispersive features in image plots. *Rev. Sci. Instrum.* **2011**, *82*, 043712.
(32) Polshyn, H.; Yankowitz, M.; Chen, S.; Zhang, Y.; Watanabe, K.; Taniguchi, T.; Dean, C. R.; Young, A. F. Large linear-in-temperature resistivity in twisted bilayer graphene. *Nat. Phys.* **2019**, *15*, 1011−1016.
(33) Kim, K.; Yankowitz, M.; Fallahazad, B.; Kang, S.; Movva, H. C. P.; Huang, S.; Larentis, S.; Corbet, C. M.; Taniguchi, T.; Watanabe, K.; Banerjee, S. K.; LeRoy, B. J.; Tutuc, E. van der Waals Heterostructures with High Accuracy Rotational Alignment. *Nano Lett.* **2016**, *16*, 1989−1995.
(34) Purdie, D. G.; Pugno, N. M.; Taniguchi, T.; Watanabe, K.; Ferrari, A. C.; Lombardo, A. Cleaning interfaces in layered materials heterostructures. *Nat. Commun.* **2018**, *9*, 5387.
(35) Volckaert, K.; Majchrzak, P.; Biswas, D.; Jones, A. J. H.; Bianchi, M.; Jiang, Z.; Dubourg, R.; Stenshøj, R. Ø.; Jensen, M. L.; Jones, N. C.; et al. Surface Electronic Structure Engineering of Manganese Bismuth Tellurides Guided by Micro-Focused Angle-Resolved Photoemission. *Adv. Mater.* **2023**, *35*, 2301907.
(36) Thompson, A. P.; Aktulga, H. M.; Berger, R.; Bolintineanu, D. S.; Brown, W. M.; Crozier, P. S.; in 't Veld, P. J.; Kohlmeyer, A.; Moore, S. G.; Nguyen, T. D.; Shan, R.; Stevens, M. J.; Tranchida, J.; Trott, C.; Plimpton, S. J. LAMMPS - a flexible simulation tool for particle-based materials modeling at the atomic, meso, and continuum scales. *Comput. Phys. Commun.* **2022**, *271*, 108171.
(37) Brenner, D. W.; Shenderova, O. A.; Harrison, J. A.; Stuart, S. J.; Ni, B.; Sinnott, S. B. A second-generation reactive empirical bond order (REBO) potential energy expression for hydrocarbons. *J. Phys.: Condens. Matter* **2002**, *14*, 783.
(38) Leconte, N.; Javvaji, S.; An, J.; Samudrala, A.; Jung, J. Relaxation effects in twisted bilayer graphene: A multiscale approach. *Phys. Rev. B* **2022**, *106*, 115410.
(39) Lee, D.; Yang, W.; Son, Y.-W.; Jung, J. Extended Hubbard corrected tight-binding model for rhombohedral few-layer graphene. *arXiv* **2024**, arXiv:2403.00530 accessed Dec 13, 2024.

(40) Jung, J.; MacDonald, A. H. Enhancement of nonlocal exchange near isolated band crossings in graphene. *Phys. Rev. B* **2011**, *84*, 085446.
(41) Nishi, H.; Matsushita, Y.-i.; Oshiyama, A. Band-unfolding approach to moiré-induced band-gap opening and Fermi level velocity reduction in twisted bilayer graphene. *Phys. Rev. B* **2017**, *95*, 085420.

https://doi.org/10.1021/acsnano.4c12905
ACS Nano 2025, 19, 2379−2387